Optica Applicata, Vol. XLVIII, No. 3, 2018
10.5277/oa180310

Multi-parameter measurement under fiber bending based on directional resonance coupling in photonic crystal fibers

Ce Tan, Qing Wang, Yi Ding, Hong-wei Li, Meng Wang, Hai Liu*

School of Information and Control Engineering, China University of Mining and Technology, Xuzhou, Jiangsu, 221116, China

*Corresponding author: lhai_hust@hotmail.com

A multi-parameter sensor with enhanced sensitivity based on magnetic fluids infiltrated photonic crystal fiber is proposed. The sensing performances are investigated using the mode coupling theory and finite element method. Four symmetrical defective channels are assembled into the photonic crystal fiber to produce two resonant transmission dips λ_{C_V} and λ_{C_H} in vertical and horizontal directions, respectively. Each dip can be split into two relatively shallow dips (λ_{CV1}, λ_{CV_2} or $\lambda_{C_{H1}}$, $\lambda_{C_{H2}}$) when the photonic crystal fiber is bent. Interestingly, the values of ($\lambda_{C_{H2}} - \lambda_{C_{H1}}$) and ($\lambda_{C_{V2}} - \lambda_{C_{V1}}$) are associated with corresponding bend-curvature but almost unaffected by external temperature or magnetic field. On the contrary, the values of ($\lambda_{C_{H2}} + \lambda_{C_{H1}}$)/2 and ($\lambda_{C_{V2}} + \lambda_{C_{V1}}$)/2 are sensitive to temperature or magnetic field regardless of the bending condition. Based on above characteristics and the dependence of the magnetic fluids refractive index on temperature and magnetic field, the proposed sensor can measure not only the bend-curvature and bend-direction, but also the temperature and magnetic field.

Keywords: fiber bending, multi-parameter measurement, photonic crystal fiber, fiber sensing.

1. Introduction

Photonic crystal fiber (PCF) has been used widely as a newly arisen platform for fiber sensing in recent years due to its own particular properties as compared with conventional fibers [1]. With the improvement of fabrication technology, PCF-based sensors have been widely used in optical fiber sensing field due to their inherent characteristics [2–4]. Although various methods are proposed for the measurement of bend-curvature, such as fiber Bragg grating (FBG) [5], long-period grating (LPG) [6, 7], multi-core fiber [8] or liquid-infiltrated PCF [9], the fiber bending condition has usually been ignored during the measurement process. As the fiber bending is often accompanied by additional variations of the temperature or strain, many effective methods are proposed to solve the cross-sensitivity problem [10, 11]. Meanwhile, some simultaneous measurement methods of the bend-curvature and other parameters are also demonstrated [12, 13].

But the point is to highlight that those behaviors are usually analyzed under a certain bending direction (*x*- or *y*-bending) [14]. So it is of great practical significance to measure the bend-direction and bend-curvature in either direction simultaneously. We intend to achieve a multi-parameter measurement under bending condition using a single PCF to make the sensing system compact and efficient. With the development of selective filling techniques, the controllable fabrication of tunable PCF devices becomes reality [15, 16]. Such PCF-based devices can be fabricated with clear spectral responses and good sensitivity [17–19].

The proposed sensor is based on a magnetic fluids-infiltrated PCF which has four symmetrical defective channels in the horizontal and vertical direction, respectively. The tunable refractive index characteristic of magnetic fluid (MF) materials is used to adjust the resonance wavelength and measure the temperature or magnetic field. The mode coupling can be controlled through the structural design of the cladding layer, and the defective channels give additional degrees of freedom that permit exploration of novel simultaneous measurement techniques. In our model, the coupling between the defect modes and the core mode would cause two transmittance dips in the spectrum due to the confinement loss. Under a certain bending direction (*x*- or *y*-bending), one dip would be split up into two shallow dips while another one remains the same. It is worth mentioning that the wavelength difference between these two dips ($\lambda_{CH2} - \lambda_{CH1}$ or $\lambda_{CV2} - \lambda_{CV1}$) is insensitive to temperature or magnetic field but sensitive to the bend -curvature. In this way, we can detect the bending angle in either direction which can be described by a two-dimensional vector. On the contrary, the average value of the two peak-wavelengths (($\lambda_{CH2} + \lambda_{CH1}$)/2 or ($\lambda_{CV2} + \lambda_{CV1}$)/2) is linear to the temperature or magnetic field without bending-induced problem. From the above characteristic, we can measure not only the bend-curvature and bend-direction, but also the temperature and magnetic field. It provides a new method to realize a PCF-based multi-parameter optical sensor which can be easily realized due to its fabricated process.

2. Model and method

The cross-section of proposed sensor is shown in Fig. 1. Four defective channels which are filled with MF materials are arranged in four directions. The structural parameters are chosen as follows: the photonic lattice period is Λ = 2.5 μm and the diameter of adjacent small air-holes is d_{air} = 1.3 μm. In addition, the values of d_1 have a significant influence on the propagation constant of core modes but make no difference to defect modes. This feature can be used to adjust the resonance wavelength to meet the need of optical fiber communication. Six bigger air-holes (d_1 = 1.62 μm) are assembled into the first layer of the PCF cladding to achieve the phase matching conditions at a particular wavelength. Another two smaller air-holes (d_2 = 0.5 μm) are designed in the second layer to modulate the energy transferring from the core to defective channels. Furthermore, the vertical and symmetrical defective channels (V_1 and V_2) are of the same diameter d_3 = 0.6 μm. Similarly, the diameter of horizontal channels (H_1 and H_2) is d_4 = 0.65 μm. When the propagation constants of core mode and defect mode are

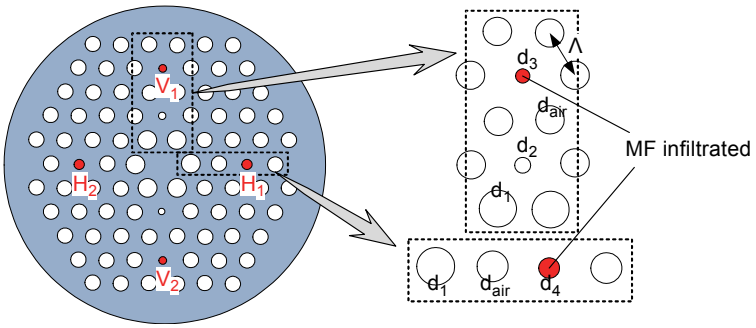

Fig. 1. The cross-section of the PCF.

equal, the energy can be transferred from the core to defective channel, and a resonant dip would appear in the transmission spectrum.

Besides, the background material is pure silica whose material dispersion relationship can be determined by the Sellimeier equation [20]:

$$n^2 = 1 + \frac{0.6961663\lambda^2}{\lambda^2 - (0.0684043)^2} + \frac{0.4079426\lambda^2}{\lambda^2 - (0.1162414)^2} + \frac{0.8974794\lambda^2}{\lambda^2 - (9.896161)^2} \quad (1)$$

Finite element method (FEM) is used to calculate the effective indices of electromagnetic mode in complex domain [21].

Figure 2 demonstrates the wavelength dependence of the effective indices of core mode and defect modes in *x*-polarized direction. Figures 2, illustrations (a) and (b) represent the optical field distributions of the hybrid mode which are the superposition of core mode and different defect modes. Figures 2, illustrations (c)–(e) indicate the op-

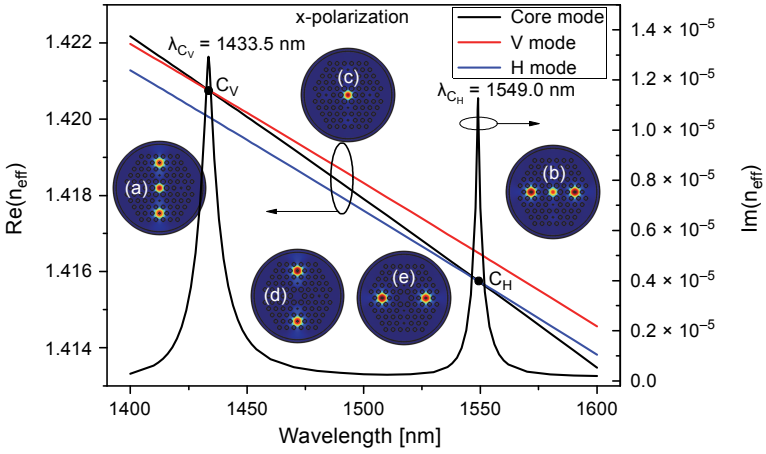

Fig. 2. Effective refractive indices of core mode and defect modes as a function of wavelength in *x*-polarized direction, and the illustrations (a)–(e) represent the optical field distributions under different coupling conditions.

tical field distribution of core mode and defect modes (V mode and H mode) at the non-resonant wavelength $\lambda = 1500$ nm, respectively. Obviously, the field of V_1 and V_2 (H_1 and H_2) are symmetrical due to their symmetrical structure, and the phase matching conditions will be satisfied at different wavelength (λ_{C_V} or λ_{C_H}). That is, the fiber core and the defective channel can form a directional coupler, and the coupling would occur at the resonant wavelength. The coupled-mode theory can be used to explain the coupling between the core mode and defect modes, and the coupling equation is expressed as follows [22]:

$$\frac{\mathrm{d}E_{\mathrm{co}}}{\mathrm{d}z} = -i\beta_{\mathrm{co}}E_{\mathrm{co}} + i\kappa_{\mathrm{co,\,de}}E_{\mathrm{de}} \tag{2a}$$

$$\frac{\mathrm{d}E_{\mathrm{de}}}{\mathrm{d}z} = -i\beta_{\mathrm{de}}E_{\mathrm{de}} + i\kappa_{\mathrm{de,\,co}}E_{\mathrm{co}} \tag{2b}$$

where $\beta_{\mathrm{co}} = k_0 n_{\mathrm{eff}}^{\mathrm{co}}$ and $\beta_{\mathrm{de}} = k_0 n_{\mathrm{eff}}^{\mathrm{de}}$ are the propagation constants of the core mode and defect mode, and $k_0 = 2\pi/\lambda$ is the wave number in free space; $k_{\mathrm{de,\,co}}$, $k_{\mathrm{co,\,de}}$ are the corresponding coupling coefficients. Then substitute $E_{\mathrm{co}} = A_{\mathrm{co}}\exp(-i\beta_{\mathrm{co}}z)$ and $E_{\mathrm{de}} = A_{\mathrm{de}}\exp(-i\beta_{\mathrm{de}}z)$ into Eqs. (2), and the normalized optical powers $P_{\mathrm{co}}(z)$ and $P_{\mathrm{de}}(z)$ can be obtained as follows:

$$P_{\mathrm{co}}(z) = \frac{|A_{\mathrm{co}}(z)|^2}{|A(0)|^2} = \frac{k_{\mathrm{co,\,de}}k_{\mathrm{de,\,co}}}{q^2}\cos^2(qz) + \frac{\delta^2}{q^2} \tag{3a}$$

$$P_{\mathrm{de}}(z) = \frac{|A_{\mathrm{de}}(z)|^2}{|A(0)|^2} = \frac{|k_{\mathrm{de,\,co}}|^2}{q^2}\sin^2(qz) \tag{3b}$$

where $q = (k_{\mathrm{co,\,de}}k_{\mathrm{de,\,co}} + \delta^2)^{1/2}$ and $\delta = (\beta_{\mathrm{de}} - \beta_{\mathrm{co}})/2$. Here, $|A_{\mathrm{co}}|^2$ and $|A_{\mathrm{de}}|^2$ represent the transmitted power in fiber core and defective waveguides, respectively. If the light is injected into the core only, the initial values can be set as $A_{\mathrm{co}}(0) = A(0)$ and $A_{\mathrm{de}}(0) = 0$. As the phase matching conditions ($n_{\mathrm{eff}}^{\mathrm{co}} = n_{\mathrm{eff}}^{\mathrm{de}}$, $\delta = 0$) are satisfied at resonance wavelength λ_{c}, $P_{\mathrm{co}}(z) = 1 - \sin^2(qz)$ and $P_{\mathrm{de}}(z) = \sin^2(qz)$.

Under the situation of $T = 20$°C and $B = 0$ mT, the effective refractive indices of different modes are obtained in Fig. 2. It can be seen that the core mode intersects with the V mode at $\lambda_{C_V} = 1433.5$ nm and the H mode at $\lambda_{C_H} = 1549.0$ nm. But at the same time, there is no intersection between the V mode and H mode. For the $\mathrm{Im}(n_{\mathrm{eff}})$ of core mode, there is a sudden change at the point of intersection (C_V or C_H), and two narrow peaks appear in the curve which can be characterized by confinement loss spectra. In other words, the fiber bending can be measured just by analyzing the confinement loss α_{CL} which is defined as:

$$\alpha_{\mathrm{CL}} = \frac{20}{\ln 10}\frac{2\pi}{\lambda}\mathrm{Im}(n_{\mathrm{eff}}) \tag{4}$$

In addition, the water-based Fe_3O_4 (concentration of 1.8%) is selected as the filling material in our model. In order to show the dependence of the MF refractive index on temperature and magnetic field, we performed the data fitting to the experimental data [23] and achieved a high linearity as

$$\Delta n_{\mathrm{MF}} = (3.4187 \times 10^{-4})\Delta B - (8.02 \times 10^{-5})\Delta T \tag{5}$$

The temperature sensitivity is figured out as 8.02×10^{-5} °C and magnetic-field sensitivity as 3.4187×10^{-4} mT. The multi-parameter sensing characteristics under bending condition would be studied in the next section.

3. Results and discussions

The experimental setup is designed as shown in Fig. 3**a**. The investigation is concentrated on the optical properties of the *x*-polarized modes, and a polarization controller (PC) is used to eliminate the *y*-polarized modes. The proposed sensor is configured by using two segments of single mode fibers (SMF) which are fixed at two graduated rotational fiber holders. Then, the device can be used to adjust the bend-direction and bend-curvature. Furthermore, a broadband source (BBS) launches the light into the PCF, and then the spectral response of output light can be observed by an optical spectrum analyzer (OSA). Figures 3**b** and 3**c** indicate the schematic diagrams for the *x*- and *y*-bending cases. When the PCF is bent, the outer part of the fiber would be stretched while the inner part is compressed. According to the photo-elastic effect, the refractive index

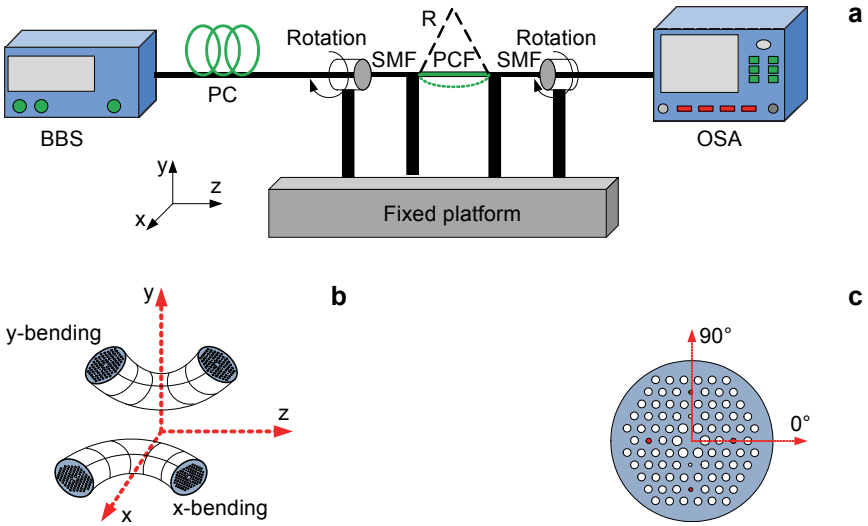

Fig. 3. The principle diagram of the experimental process (**a**), the schematic diagrams of bending process (**b**), and the direction angle for *x*- and *y*-bending (**c**).

of the outside layers would become smaller but that of inside layers would be contrary. To simplify the calculation, an equivalent index profile can be expressed as [24]:

$$n'(x, y) = n(x, y)(1 + Cx) \tag{6a}$$

$$n'(x, y) = n(x, y)(1 + Cy) \tag{6b}$$

where $C = 1/R$ is the bend-curvature, $n(x, y)$ and $n'(x, y)$ are the refractive index profiles before and after the fiber is bent, respectively. In order to have a more precise and practical investigation, both of the thermo-optic effect and thermal expansion effect are considered. The thermo-optic coefficients are taken as $\xi_{SiO_2} = 7.0 \times 10^{-6}$, and the thermal-expansion coefficients are chosen as $\alpha_{SiO_2} = 0.55 \times 10^{-6}$.

Firstly, we calculated the confinement loss of core mode under the condition of $T = 20°C$ and $B = 0$ mT, and obtained the spectral response with different bend-directions as shown in Fig. 4. For x-bending case, the resonant peak λ_{C_H} is split up into two

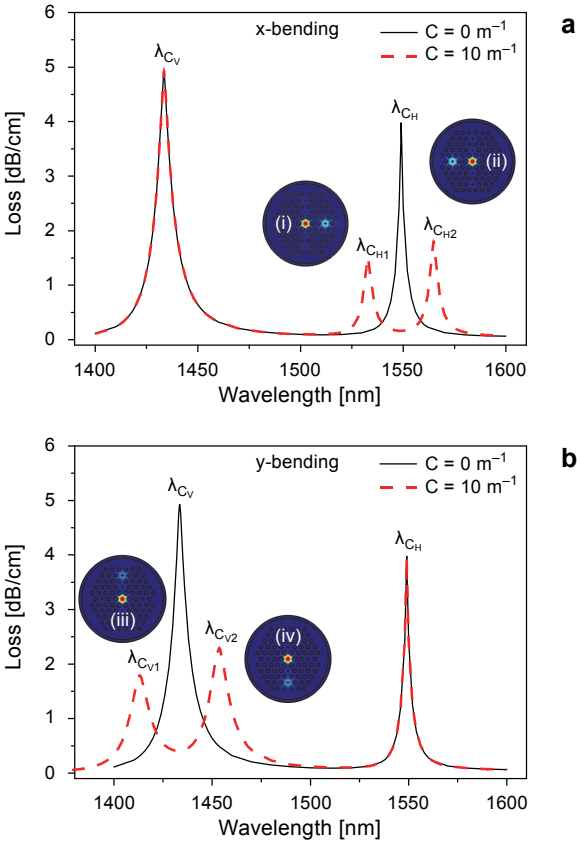

Fig. 4. Loss spectra of core mode for x-bending (**a**) and y-bending (**b**) when bend-curvature $C = 0$ m^{-1} and $C = 10$ m^{-1}.

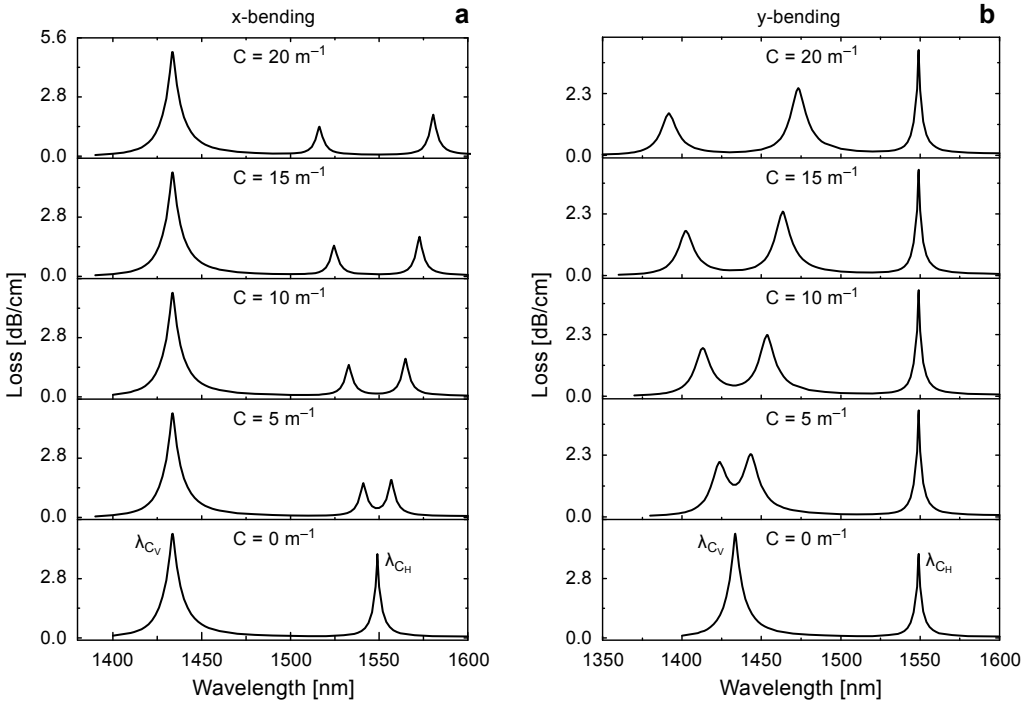

Fig. 5. Loss spectra with different bend-curvatures C for x-bending (**a**) and y-bending (**b**) under the condition of $T = 20$°C and $B = 0$ mT.

shallow peaks $\lambda_{C_{H1}}$ and $\lambda_{C_{H2}}$ while another peak λ_{C_V} remains unchanged. Similarly, for y-bending case, the resonant peak λ_{C_V} would be split up into two shallow peaks while the peak λ_{C_H} is keeping steady. The inserts in Fig. 4 present the hybrid field of core mode and different defect modes, respectively. Then, the loss spectra with different bend-curvatures are obtained in Fig. 5. For x-bending case, there is a blue-shift for the resonant peak $\lambda_{C_{H1}}$ and a red-shift for $\lambda_{C_{H2}}$ when the bend-curvature increases from 0 to 20 m^{-1}. Similarly, the peak $\lambda_{C_{V1}}$ has a blue-shift while the peaks $\lambda_{C_{V2}}$ and λ_{C_H} remain steady for y-bending case. Thus, the relationship between resonant loss peak-shift and the bend-direction can be characterized.

Here, we consider the case of $C = 0$ m^{-1} as the reference value, and the curvature sensitivities for different bend-directions can be calculated from Fig. 6. The sensitivities are $k_{H_1} = -1.636$ nm/m^{-1}, $k_{H_2} = 1.576$ nm/m^{-1} and $k_{\Delta\lambda_H} = 3.212$ nm/m^{-1} for x-bending case, and $k_{V_1} = -2.096$ nm/m^{-1}, $k_{V_2} = 2.011$ nm/m^{-1} and $k_{\Delta\lambda_V} = 4.086$ nm/m^{-1} for y-bending case. Since the PCF is selectively filled with MF material, we intend to verify the wavelength difference between the two shallow dips not affected by the temperature or magnetic field. Five random sampling points (B [mT], T [°C], C [m^{-1}]) are selected to simulate the process and the results are listed in Table 1. Then, the slopes

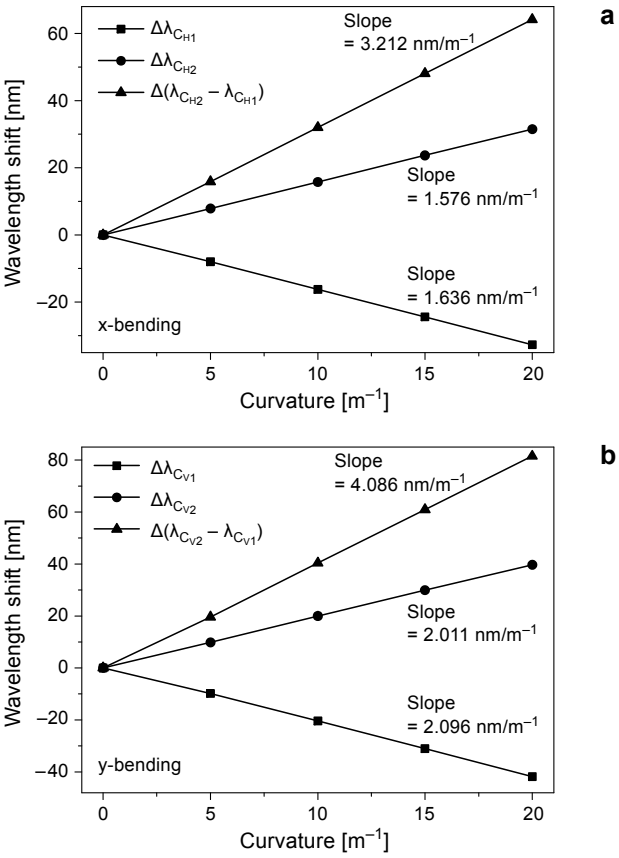

Fig. 6. Relationship between the peak-shifts and bend-curvature C for different splitting peaks under x-bending (**a**) and y-bending (**b**) conditions.

T a b l e 1. Peak-shifts at different random temperatures and magnetic fields.

Sampling points			x-bending			y-bending		
B [mT]	T [°C]	C [m^{-1}]	λ_{C_V} [nm]	$\lambda_{C_{H1}}$ [nm]	$\lambda_{C_{H2}}$ [nm]	$\lambda_{C_{V1}}$ [nm]	$\lambda_{C_{V2}}$ [nm]	λ_{C_H} [nm]
0	20	0	1433.5	1549	1549	1433.5	1433.5	1549
8	54	5	1434.5	1542.1	1557.9	1424.7	1444.3	1550.1
24	40	10	1392.7	1488.6	1520.6	1372.3	1412.7	1504.8
14	72	15	1431.2	1522.1	1570.2	1400.2	1461.1	1546.5
42	36	20	1352.0	1428.1	1492.3	1310.2	1391.7	1460.8

of the best-fit lines for $\Delta(\lambda_{C_{H2}} - \lambda_{C_{H1}})$ and $\Delta(\lambda_{C_{V2}} - \lambda_{C_{V1}})$ can be obtained from Fig. 7, which are consistent with the values from Fig. 6. That is, our proposed curvature sensor can be insensitive to ambient temperature and magnetic field.

For convenience, we define $S_H = (\lambda_{C_{H2}} - \lambda_{C_{H1}})/C$ and $S_V = (\lambda_{C_{V2}} - \lambda_{C_{V1}})/C$ to represent the curvature sensitivity for two orthogonal bend-directions. Assuming that the

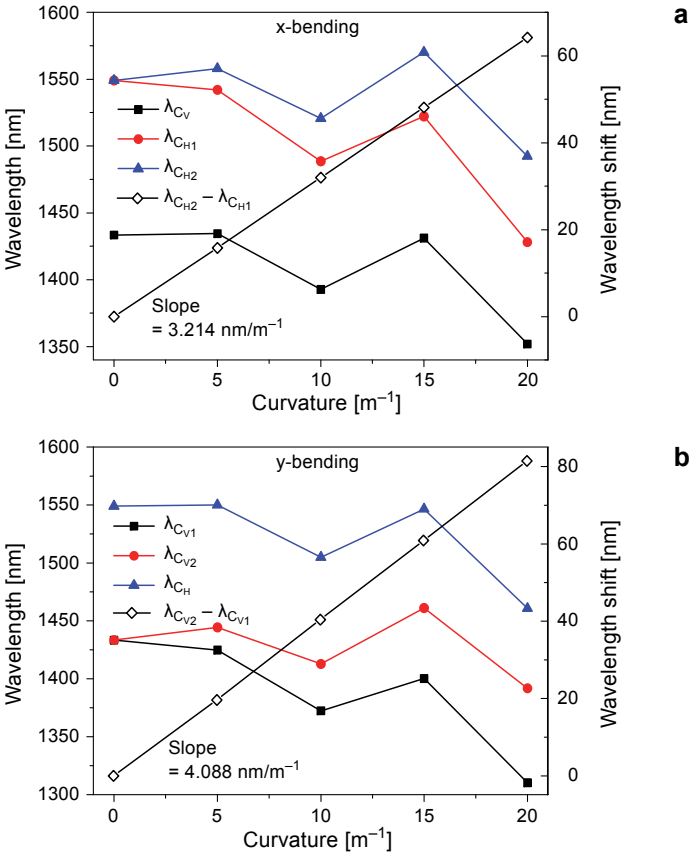

Fig. 7. Relationship between the peak-shifts and bend-curvature C for x-bending (**a**) and y-bending (**b**) with random temperatures T and magnetic fields B.

PCF is bent slightly in either direction, the curvature also can be decomposed into two components in the x- and y-directions, respectively [25]. Therefore, a two-dimensional vector is proposed to explore the bending angle θ which can be expressed as:

$$C^2 = C_x^2 + C_y^2 = \left(\frac{\lambda_{C_{H2}} - \lambda_{C_{H1}}}{S_H}\right)^2 + \left(\frac{\lambda_{C_{V2}} - \lambda_{C_{V1}}}{S_V}\right)^2 \tag{7}$$

$$\theta = \arctan\left(\frac{C_y}{C_x}\right) = \arctan\left(\frac{S_H}{S_V}\frac{\lambda_{C_{V2}} - \lambda_{C_{V1}}}{\lambda_{C_{H2}} - \lambda_{C_{H1}}}\right) \tag{8}$$

And then, the bend-direction and bend-curvature can be detected simultaneously by measuring the wavelength-shifts of $\lambda_{C_{H1}}$, $\lambda_{C_{H2}}$, $\lambda_{C_{V1}}$ and $\lambda_{C_{V2}}$ separately.

Next, a random bending condition $C = 12$ m^{-1} and $\theta = 60°$ (actual value) is selected as another example. Figure 8 shows the loss spectrum of the core mode, $\Delta\lambda_{C_V} = 42.1$ nm and $\Delta\lambda_{C_H} = 19.1$ nm. Then, the bend-direction $\theta = 60.02°$ and the bend-curvature

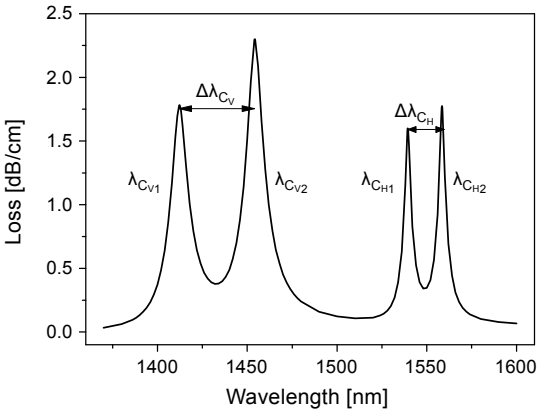

Fig. 8. The confinement loss spectrum of the core mode under the condition of $C = 12$ m^{-1} and $\theta = 60°$.

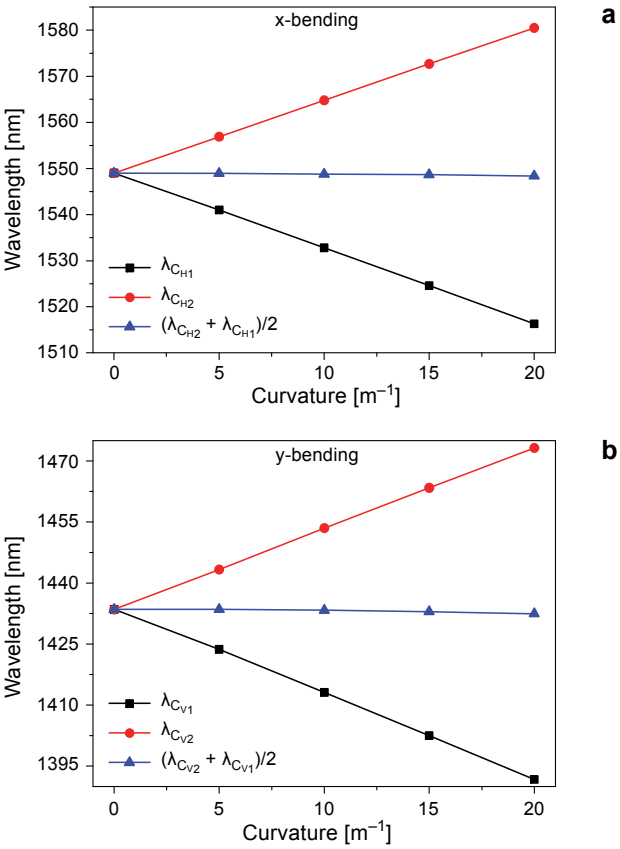

Fig. 9. Relationship between the peak-shifts and bend-curvature C for the average value of two splitting peaks under x-bending (**a**) and y-bending (**b**) conditions.

$C = 11.90\ \mathrm{m}^{-1}$ (calculated value) can be obtained from Eqs. (7) and (8). The calculated results proved the feasibility and effectiveness of our proposed method.

More interesting, as is shown in Fig. 9, the values of $\lambda'_{C_H} = (\lambda_{CH1} + \lambda_{CH2})/2$ and $\lambda'_{C_V} = (\lambda_{CV1} + \lambda_{CV2})/2$ remain unchanged basically, while the bend-curvature varies from 0 to 20 m^{-1} under the condition of $T = 20°\mathrm{C}$ and $B = 0$ mT. In other words, λ'_{C_H} and λ'_{C_V} are insensitive to the bend-curvature. This feature can be used to measure the temperature and magnetic field without the bending-induced effect. As a result, the temperature and magnetic field can be obtained simultaneously using the following inverse matrices

$$\begin{bmatrix} \Delta T \\ \Delta B \end{bmatrix} = \begin{bmatrix} k_1 & k_2 \\ k_3 & k_4 \end{bmatrix}^{-1} \begin{bmatrix} \Delta\lambda'_{C_V} \\ \Delta\lambda'_{C_H} \end{bmatrix} \tag{9}$$

The elements of the coefficient matrix can be determined by measuring the wavelength-shifts separately.

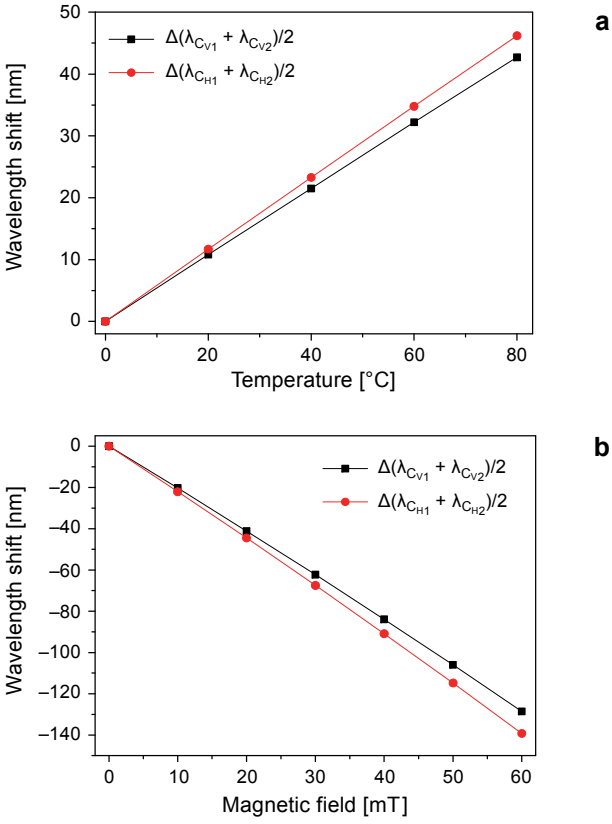

Fig. 10. The sensitivity of temperature (**a**) and magnetic field (**b**) under the condition of $C = 0\ \mathrm{m}^{-1}$.

T a b l e 2. Wavelength-shifts with different conditions (state I, II and III) as an example.

Sampling points	Wavelength [nm]			
(B [mT], T [°C], C [m^{-1}], θ [°])	$(\lambda_{C_{V2}} + \lambda_{C_{V1}})/2$	$(\lambda_{C_{H2}} + \lambda_{C_{H1}})/2$	$\lambda_{C_{V2}} - \lambda_{C_{V1}}$	$\lambda_{C_{H2}} - \lambda_{C_{H1}}$
I = (18, 54, 10, 45)	1414.16	1528.08	28.8	22.9
II = (8, 72, 6, 30)	1444.70	1561.13	11.5	16.3
III = (32, 15, 14, 60)	1363.18	1472.90	50.4	23.2
	Calculated value			
	C	θ	ΔB	ΔT
I = (18, 54, 10, 45)	10.03	44.67	–9.73 (I → II)	18.10 (I → II)
II = (8, 72, 6, 30)	5.80	29.01	23.76 (II → III)	–57.24 (II → III)
III = (32, 15, 14, 60)	14.29	59.65	14.03 (I → III)	–39.14 (I → III)

Without loss of generality, the sensitivities of temperature and magnetic field under the condition of $C = 0$ m^{-1} are obtained in Fig. 10. The elements of coefficient matrix K are determined as $k_1 = 0.534$ nm/°C, $k_2 = –2.143$ nm/mT, $k_3 = 0.578$ nm/°C, and $k_4 = –2.319$ nm/mT.

If the ambient conditions vary randomly in the sensing process, we need to define a four-dimensional vector (B, T, C, θ) to describe the sampling process. Three sampling points (I = (18 mT, 54°C, 10 m^{-1}, 45°), II = (8 mT, 72°C, 6 m^{-1}, 30°), and III = (32 mT, 15°C, 14 m^{-1}, 60°)) are selected as an example. The loss peak-shifts under the three conditions are listed in Table 2, and the calculated results also show a very good agreement with the actual values. The proposed sensor can measure not only the bend-curvature and bend-direction, but also the temperature and magnetic field.

4. Conclusion

In conclusion, a multi-parameter PCF sensor under fiber bending condition is proposed. Based on the flexible design of PCF, the simultaneous measurement of bend-curvature and bend-direction can avoid being influenced by the temperature or magnetic field. In the meantime, the temperature and magnetic field also can be discriminated regardless of the bending-induced effect. Thereby, the proposed sensor is considered to be an excellent candidate for multifunctional measurement under different fiber bending conditions.

Acknowledgements – Supported by the National Natural Science Foundation of China under grant No. 51874301, National Key R&D Program of China under grant No. 2016YFC0801800 and No. 2017YFF0205500, Science and Technology Innovation Project of Xuzhou city under grant No. KC16SG264 and the Special Foundation for Excellent Young Teachers and Principals Program of Jiangsu Province, China.

References

[1] RUSSELL P., *Photonic crystal fibers*, Science 299(5605), 2003, pp. 358–362.

[2] Hai Liu, Ce Tan, Chenghao Zhu, Yan Wang, Hanlin Ma, *Multi-parameters measurement based on cascaded Bragg gratings in magnetic fluid-infiltrated photonic crystal fibre*, Journal of Modern Optics 64(8), 2017, pp. 887–894.

[3] Huaping Gong, Haifeng Song, Sulei Zhang, Yongxing Jin, Xinyong Dong, *Curvature sensor based on hollow-core photonic crystal fiber Sagnac interferometer*, IEEE Sensors Journal 14(3), 2014, pp. 777–780.

[4] Hai Liu, Chenghao Zhu, Yan Wang, Ce Tan, Hongwei Li, Deqiang Cheng, *Polarization-dependent transverse-stress sensing based on photonic crystal fiber with gold-coated air-holes*, Optical Engineering 56(5), 2017, article ID 057112.

[5] Zhifang Wu, Yan-Ge Liu, Zhi Wang, Meng Jiang, Wenbin Ji, Tingting Han, Shuo Li, Xuguang Shao, Xuan Quyen Dinh, Swee Chuan Tjin, Perry Ping Shum, *Simultaneous measurement of curvature and strain based on fiber Bragg grating in two-dimensional waveguide array fiber*, Optics Letters 38(20), 2013, pp. 4070–4073.

[6] Xianlun Yu, Weidong Gao, Yong Qu, Shunjun Shu, *The design of bending long period of photonic crystal fiber grating sensors*, Optics and Photonics Journal 6(8B), 2016, pp. 120–126.

[7] Wenjun Ni, Ping Lu, Chao Luo, Xin Fu, Li Liu, Hao Liao, Xinyue Jiang, Deming Liu, Jiangshan Zhang, *Bending direction detective fiber sensor for dual-parameter sensing based on an asymmetrical thin-core long-period fiber grating*, IEEE Photonics Journal 8(4), 2016, article ID 6803811.

[8] Silva R.M., Ferreira M.S., Kobelke J., Schuster K., Frazão O., *Simultaneous measurement of curvature and strain using a suspended multicore fiber*, Optics Letters 36(19), 2011, pp. 3939–3941.

[9] Chen H.F., Ying Wang, Wang D.N., *Selectively infiltrated PCF for directional bend sensing with large bending range*, IEEE Photonics Technology Letters 27(5), 2015, pp. 502–505.

[10] Xinyong Dong, Yang Liu, Li-Yang Shao, Juan Kang, Chun-Liu Zhao, *Temperature-independent fiber bending sensor based on a superimposed grating*, IEEE Sensors Journal 11(11), 2011, pp. 3019–3022.

[11] Villatoro J., Van Newkirk A., Antonio-Lopez E., Zubia J., Schülzgen A., Amezcua-Correa R., *Ultrasensitive vector bending sensor based on multicore optical fiber*, Optics Letters 41(4), 2016, pp. 832–835.

[12] Dash J.N., Dass S., Jha R., *Photonic crystal fiber microcavity based bend and temperature sensor using micro fiber*, Sensors and Actuators A: Physical 244, 2016, pp. 24–29.

[13] Jing Kong, Xiaowei Ouyang, Ai Zhou, Libo Yuan, *Simultaneous strain and directional bending sensor based on eccentric-core fiber Bragg grating*, Proceedings of SPIE 10323, 2017, article ID 1032378.

[14] Chen D., Hu G., Liu X.A., Peng B., Wu G., *Bending analysis of a dual-core photonic crystal fiber*, Progress In Electromagnetics Research 120, 2011, pp. 293–307.

[15] Ying Wang, Liao C.R., Wang D.N., *Femtosecond laser-assisted selective infiltration of microstructured optical fibers*, Optics Express 18(17), 2010, pp. 18056–18060.

[16] Fei Wang, Wu Yuan, Ole Hansen, Ole Bang, *Selective filling of photonic crystal fibers using focused ion beam milled microchannels*, Optics Express 19(18), 2011, pp. 17585–17590.

[17] Hai Liu, Ce Tan, Chenghao Zhu, Yan Wang, Yuan Gao, Hanlin Ma, Deqiang Cheng, *Simultaneous measurement of temperature and magnetic field based on directional resonance coupling in photonic crystal fibers*, Optics Communications 391, 2017, pp. 111–115.

[18] Qiang Liu, Shuguang Li, Hailiang Chen, Zhenkai Fan, Jianshe Li, *Photonic crystal fiber temperature sensor based on coupling between liquid-core mode and defect mode*, IEEE Photonics Journal 7(2), 2015, article ID 4500509.

[19] Hameed M.F.O., Azab M.Y., Heikal A.M., El-Hefnawy S.M., Obayya S.S.A., *Highly sensitive plasmonic photonic crystal temperature sensor filled with liquid crystal*, IEEE Photonics Technology Letters 28(1), 2016, pp. 59–62.

[20] Tatian B., *Fitting refractive-index data with the Sellmeier dispersion formula*, Applied Optics 23(24), 1984, pp. 4477–4485.

[21] SAITOH K., KOSHIBA M., *Full-vectorial imaginary-distance beam propagation method based on a finite element scheme: application to photonic crystal fibers*, IEEE Journal of Quantum Electronics 38(7), 2002, pp. 927–933.

[22] WU D.K.C., KWANG JO LEE, PUREUR V., KUHLMEY B.T., *Performance of refractive index sensors based on directional couplers in photonic crystal fibers*, Journal of Lightwave Technology 31(22), 2013, pp. 3500–3510.

[23] YONG ZHAO, DI WU, RI-QING LV, YU YING, *Tunable characteristics and mechanism analysis of the magnetic fluid refractive index with applied magnetic field*, IEEE Transactions on Magnetics 50(8), 2014, article ID 4600205.

[24] NGOC HAI VU, IN-KAG HWANG, YONG-HEE LEE, *Bending loss analyses of photonic crystal fibers based on the finite-difference time-domain method*, Optics Letters 33(2), 2008, pp. 119–121.

[25] CHEN HUIFANG, YAN HUIMIN, SHAN GUOFENG, *Design of two-dimensional bending vector sensor based on selective infiltration of photonic crystal fiber*, Chinese Journal of Lasers **43**(1), 2015, article ID 0105003.

Received September 2, 2017